Structure and lattice dynamics of the wide band gap semiconductors $MgSiN_2$ and $MgGeN_2$

M. Råsander, J. B. Quirk, T. Wang, S. Mathew, R. Davies, R. G. Palgrave, and M. A. Moram

Citation: Journal of Applied Physics **122**, 085705 (2017);
View online: https://doi.org/10.1063/1.4985775
View Table of Contents: http://aip.scitation.org/toc/jap/122/8
Published by the American Institute of Physics

Articles you may be interested in

Structural and electrical properties of single crystalline $SrZrO_3$ epitaxially grown on Ge (001)
Journal of Applied Physics **122**, 084102 (2017); 10.1063/1.5000142

Enhanced room temperature ferromagnetism in Ni doped SnO_2 nanoparticles: A comprehensive study
Journal of Applied Physics **122**, 083906 (2017); 10.1063/1.4999830

Electronic band structures and excitonic properties of delafossites: A GW-BSE study
Journal of Applied Physics **122**, 085104 (2017); 10.1063/1.4991913

First-principles and molecular dynamics study of thermoelectric transport properties of N-type silicon-based superlattice-nanocrystalline heterostructures
Journal of Applied Physics **122**, 085105 (2017); 10.1063/1.5000356

Influence of the heterostructure design on the optical properties of GaN and $Al_{0.1}Ga_{0.9}N$ quantum dots for ultraviolet emission
Journal of Applied Physics **122**, 085706 (2017); 10.1063/1.5000238

Effects of thickness ratio of InGaN to GaN in superlattice strain relief layer on the optoelectrical properties of InGaN-based green LEDs grown on Si substrates
Journal of Applied Physics **122**, 084504 (2017); 10.1063/1.5000134

Scilight
Sharp, quick summaries illuminating the latest physics research
Sign up for FREE!
AIP Publishing

JOURNAL OF APPLIED PHYSICS **122**, 085705 (2017)

Structure and lattice dynamics of the wide band gap semiconductors $MgSiN_2$ and $MgGeN_2$

M. Råsander,[1,a)] J. B. Quirk,[1] T. Wang,[1] S. Mathew,[2] R. Davies,[1] R. G. Palgrave,[2] and M. A. Moram[1]
[1]*Department of Materials, Imperial College London, Exhibition Road, SW7 2AZ London, United Kingdom*
[2]*Department of Chemistry, University College London, Gordon Street, WC1H 0AJ London, United Kingdom*

(Received 16 May 2017; accepted 11 August 2017; published online 30 August 2017)

We have determined the structural and lattice dynamical properties of the orthorhombic, wide band gap semiconductors $MgSiN_2$ and $MgGeN_2$ using density functional theory. In addition, we present the structural properties and Raman spectra of $MgSiN_2$ powder. The structural properties and lattice dynamics of the orthorhombic systems are compared to those of wurtzite AlN. We find clear differences in the lattice dynamics between $MgSiN_2$, $MgGeN_2$ and AlN, for example, we find that the highest phonon frequency in $MgSiN_2$ is about 100 cm^{-1} higher than the highest frequency in AlN, and that $MgGeN_2$ is much softer. We also provide the Born effective charge tensors and dielectric tensors of $MgSiN_2$, $MgGeN_2$ and AlN. Phonon related thermodynamic properties, such as the heat capacity and the entropy, have also been evaluated and are found to be in very good agreement with available experimental results. *Published by AIP Publishing.*
[http://dx.doi.org/10.1063/1.4985775]

I. INTRODUCTION

Group III-nitride semiconductors AlN, GaN and InN are widely used in optoelectronic and high power electronic devices.[1–3] AlN and its alloys are also widely used in energy harvesting devices and RF applications.[4] However, improved efficiencies are required for III-nitride-based ultraviolet (UV) light emitting diodes,[5] solar cells[6] and energy harvesting devices.[4] Group II-IV nitride semiconductors are of growing interest in this regard, as their bonding and crystal structures are related to those of III-nitrides, but they offer different combinations of band gaps and lattice parameters, opening up additional possibilities for device design.[7,8] For example, Zn-based II-IV nitrides are of current interest for solar cells,[7,8] whereas wide band gap II-IV nitrides, such as $MgSiN_2$, may find applications as part of UV optoelectronic devices.[9–11]

$MgSiN_2$ and $MgGeN_2$ have been found to possess a wurtzite-derived orthorhombic crystal structure which belongs to the $Pna2_1$ space group (No. 33).[12] The band gap of $MgSiN_2$ has been investigated by both theory[9–11,13–15] and experiment,[9,15,16] and it has been found that the band gap in $MgSiN_2$ is indirect with a similar size as the band gap in wurtzite AlN.[9,11,15] A recent study employing the GW approximation has established that the band gap decreases from 5.85 eV in $MgSiN_2$ to 5.14 eV in $MgGeN_2$ to 3.43 eV in $MgSnN_2$ when the Group IV element is substituted from Si to Ge to Sn.[11] It was also found that the band gaps in both $MgGeN_2$ and $MgSnN_2$ are direct, in contrast to the indirect gap in $MgSiN_2$. A similar trend is also observed for Zn-IV-N_2 nitride phases,[7,8] however, the sizes of the band gaps are smaller in these Zn-based systems than in the equivalent Mg-based II-IV nitrides. In addition to having a large band gap, $MgSiN_2$ has been found to possess a small anisotropic thermal expansion,[17] and a thermal conductivity of 28 W/mK was obtained for the powder at 300 K.[18] These properties together with the great lattice matching between $MgSiN_2$ and AlN[9] suggest that $MgSiN_2$ could be used for short wavelength or high power electronic devices where heat transport away from the active region of the device is highly desirable.

Even though the understanding of the electronic properties of the Mg-IV-N_2 systems is increasing, not much is known regarding the lattice dynamics and related properties. Apart from experimental studies of thermal expansion,[17] thermal conductivity[18] and heat capacity[19] of $MgSiN_2$, there are two recent theoretical studies focusing on phonon related properties: Arab *et al.*[20] used a simple quasi-harmonic Debye model to evaluate the thermodynamic properties of $MgSiN_2$, while Pramchu *et al.*[21] used density functional perturbation theory in combination with the local density approximation to evaluate the phonon dispersions of both $MgSiN_2$ and $MgGeN_2$. However, neither of these studies provide a connection between the lattice dynamics and the thermodynamic properties of these compounds. In this study, we present structural as well as phonon-related properties, such as phonon dispersions, phonon density of states, Helmholtz free energy and heat capacity, of $MgSiN_2$ and $MgGeN_2$ to provide a connection between the structure, the lattice dynamics and the thermodynamic properties of these systems. The bulk of the results presented here is obtained using calculations based on density functional theory. However, we also provide experimental structural properties and Raman spectra of $MgSiN_2$ powder. In order to facilitate greater understanding, the properties established for $MgSiN_2$ and $MgGeN_2$ will be compared with those of wurtzite AlN, which is the starting point for obtaining the crystal structure of $MgSiN_2$. We note that both $MgSiN_2$ and $MgGeN_2$ have been produced in powder form previously,[12] and,

---

[a)] Electronic mail: m.rasander@imperial.ac.uk considering the size of the band gaps,[11] are of interest in UV-optoelectronic applications.

II. METHOD

Density functional calculations have been performed using the projector augmented wave (PAW) method[22] as implemented in the Vienna *ab initio* simulation package (VASP).[23,24] We have used the generalized gradient approximation of Perdew, Burke and Ernzerhof (PBE)[25] for the exchange-correlation energy functional. The plane wave energy cut-off was set to 800 eV, and we have used Γ-centered k-point meshes with the smallest allowed spacing between k-points of 0.1 Å^{-1}. The atomic positions and the simulation cell shapes were relaxed until the Hellmann-Feynman forces acting on atoms were smaller than 0.0001 eV/Å. Furthermore, we have used the standard core-valence partitioning for Mg (with a $3s^2$ valence), Si (with a $3s^23p^2$ valence), Al (with a $3s^23p^1$ valence) and N (with a $2s^22p^3$ valence). In the case of Ge, we have used both the four 4s and 4p electrons and the semi-core 3d electrons as valence states.

The evaluation of phonon related properties has been done using the finite displacement method as it is implemented in the Phonopy code.[26,27] For $MgSiN_2$ and $MgGeN_2$, we have used supercells based on a $3 \times 3 \times 3$ repetition of the primitive orthorhombic unit cells containing 432 atoms. In the case of AlN, we have used a $5 \times 5 \times 4$ repetition of the primitive wurtzite unit cell with 400 atoms in the supercell. The phonon density of states and the related properties were obtained using a $24 \times 24 \times 24$ q-point mesh for $MgSiN_2$ and $MgGeN_2$ and a $48 \times 48 \times 48$ q-point mesh for AlN.

In polar crystals, a macroscopic electric field is induced by the collective displacement of the ions at $\boldsymbol{q} = 0$. This electric field affects the longitudinal optical (LO) modes and not the transverse optical (TO) modes, and therefore gives rise to a LO-TO splitting of the modes when approaching the Γ-point. To account for this effect, a non-analytical correction to the dynamical matrix of the form

$$D^{NA}_{\alpha j,\beta j'}(\boldsymbol{q} \to 0) = \frac{4\pi}{\Omega_0\sqrt{m_j m_{j'}}} \frac{\left[\sum_\gamma q_\gamma \boldsymbol{Z}^*_{j,\gamma\alpha}\right]\left[\sum_{\gamma'} q_{\gamma'} \boldsymbol{Z}^*_{j',\gamma'\beta}\right]}{\sum_{\alpha\beta} q_\alpha \boldsymbol{\varepsilon}^\infty_{\alpha\beta} q_\beta} \quad (1)$$

is added.[28–31] Here, $\boldsymbol{\varepsilon}^\infty$ is the high-frequency dielectric tensor and $\boldsymbol{Z}^*_s$ is the Born effective charge tensor for the atom s. The dielectric tensors and Born effective charge tensors of $MgSiN_2$, $MgGeN_2$ and AlN were calculated using density functional perturbation theory,[32] as outlined by Gajdoš *et al.*[33]

In addition, $MgSiN_2$ powders were synthesised by firing stoichiometric Mg and Si_3N_4 powders in a horizontal tube furnace for 16 h at 1000 °C at a heating rate of 10 °C/min under a flowing N_2 (700 sccm) atmosphere in a Mo boat, prior to cooling at 5 °C/min. To verify the crystal structure, powder X-ray diffraction (XRD) was performed over the range 20°–120° 2θ, using Cu-Kα_1 radiation. Furthermore, Raman measurements were collected using a LabRAM HR Evolution spectrometer (Horiba Scientific) using a laser wavelength of 532 nm, an objective lens of ×10, and a grating of 600 lines/mm. Spectra were recorded over the wavenumber range 100 to 1250 cm^{-1} with an acquisition time of 100 s.

III. STRUCTURAL PROPERTIES

The ordered $MgSiN_2$ and $MgGeN_2$ structures can be derived from the AlN structure by substituting one Mg and one Si (or Ge) atom for every two Al atoms. The structures have been found to be orthorhombic and belong to the $Pna2_1$ space group (No. 33),[12,17] where all atoms occupy the 4*a* Wyckoff crystal positions, and the unit cell, therefore, contains 4 formula units of $MgSiN_2$ or $MgGeN_2$. The crystal structure is shown in Fig. 1, and the structural parameters are presented in Table I for $MgSiN_2$ and in Table II for $MgGeN_2$. We note that in this structure, there are two different nitrogen positions, labelled N(1) and N(2). The N(1) positions are approximately positioned above the Si (or Ge) positions along the *c*-axis, while the N(2) positions are approximately positioned above the Mg positions. In order to satisfy local charge neutrality, each of the N(1) and N(2) positions has two Mg and two Si (or Ge) atoms as the nearest neighbours. Correspondingly, each of the Mg and Si (or Ge) positions has two N(1) and two N(2) positions as the nearest neighbours.

In Fig. 2, we show the measured XRD pattern of $MgSiN_2$, which shows that the structure is orthorhombic and belongs to the $Pna2_1$ space group. We also find peaks related to pure Si and MgO impurities in the sample. The corresponding $MgSiN_2$ lattice constants are shown in Table I. The measured lattice constants are in very good agreement with previously measured lattice constants.[17]

As shown in Tables I and II, we find that the PBE calculations overestimate the lattice constants compared to available experiments, with a maximum deviation of 0.9% for $MgSiN_2$ and 1.1% for $MgGeN_2$, which is to be expected using the PBE approximation for these types of systems.[34] The calculated structural parameters are also in agreement

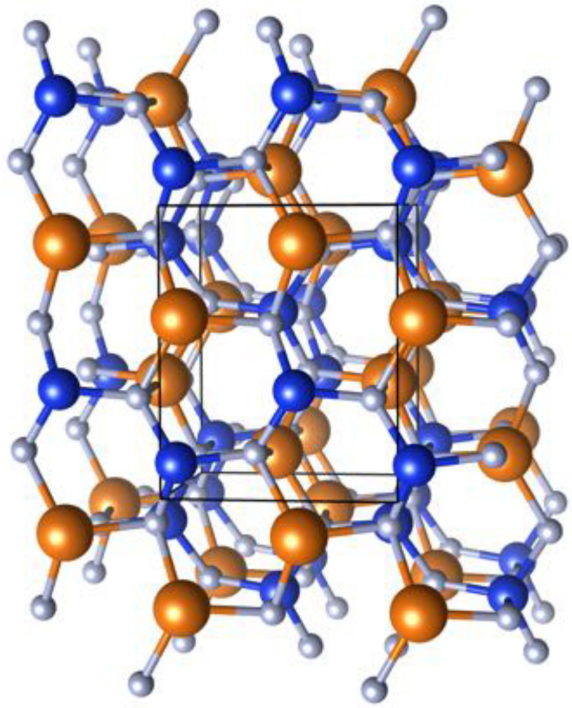

FIG. 1. The orthorhombic crystal structure (space group $Pna2_1$) of $MgSiN_2$ and $MgGeN_2$. Mg is represented by the large bronze colored spheres, Si (or Ge) is represented by blue spheres, while N is represented by small grey spheres.

TABLE I. Lattice constants and crystallographic coordinates (x, y, z) of orthorhombic $MgSiN_2$. The numbers in parenthesis are the deviation from the experimental value.

XC	a (Å)	b (Å)	c (Å)
PBE	5.311 (0.8%)	6.495 (0.4%)	5.028 (0.9%)
Expt. ($T = 300$ K)	5.314	6.466	4.975
Expt. ($T = 10$ K)[17]	5.27078(5)	6.46916(7)	4.98401(5)
		PBE	
	x	y	z
Mg	0.0849	0.6228	0.9886
Si	0.0700	0.1254	0.0000
N(1)	0.0485	0.0957	0.3471
N(2)	0.1093	0.6553	0.4102
		Expt. ($T = 10$ K)[17]	
	x	y	z
Mg	0.08448(34)	0.62255(30)	0.9866(5)
Si	0.0693(5)	0.1249(4)	0.0000
N(1)	0.04855(17)	0.09562(15)	0.3472(4)
N(2)	0.10859(18)	0.65527(14)	0.4102(4)

with previous results obtained using local and semi-local approximations for the exchange-correlation energy functional.[11,13,14] We note that $MgGeN_2$ has a unit cell volume of 192.96 Å^3 (12.06 Å^3/atom), while the corresponding volume of $MgSiN_2$ is 173.44 Å^3 (10.84 Å^3/atom). $MgGeN_2$ is, therefore, a larger crystal than $MgSiN_2$ and, due to the larger mass of Ge compared to Si, the mass density of $MgGeN_2$ is also larger than in $MgSiN_2$. In the case of wurtzite AlN, the calculated structural parameters are $a = 3.127$ Å, $c = 5.013$ Å and $u = 0.382$, which are in good agreement with experiment. When comparing the volume per atom of $MgSiN_2$ with that of AlN, we find that the volume of $MgSiN_2$ is slightly larger at 10.84 Å^3/atom compared to 10.61 Å^3/atom in the case of AlN, which leads to the mass density being larger in AlN than in $MgSiN_2$.

TABLE II. Lattice constants and crystallographic coordinates (x, y, z) of orthorhombic $MgGeN_2$. The numbers in parenthesis are the deviation from the experimental value.

XC	a (Å)	b (Å)	c (Å)
PBE	5.549 (1.0%)	6.658 (0.7%)	5.223 (1.1%)
Expt. [12]	5.494	6.611	5.166
		PBE	
	x	y	z
Mg	0.0851	0.6234	0.9929
Ge	0.0736	0.1258	0.0000
N(1)	0.0604	0.1073	0.3600
N(2)	0.1002	0.6431	0.3975
		Expt.[12]	
	x	y	z
Mg	0.083	0.625	0.000
Ge	0.083	0.125	0.000
N(1)	0.083	0.125	0.380
N(2)	0.083	0.625	0.400

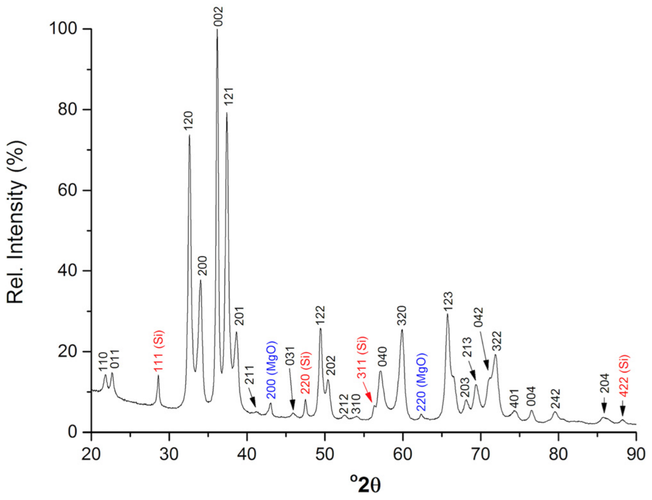

FIG. 2. Measured X-ray diffractogram of $MgSiN_2$ powder, indexed as the ordered orthorhombic structure belonging to the Pna2_1 space group. Peaks corresponding to the MgO and Si impurity phases are highlighted using blue and red colours, respectively.

In $MgSiN_2$ and $MgGeN_2$, all atoms are locally found in a distorted tetrahedral environment, which has been discussed in detail by Bruls *et al.*[17] For $MgSiN_2$, we obtain average Mg-N and Si-N binding distances of 2.11 Å and 1.76 Å, respectively, which are slightly larger than 2.09 Å and 1.75 Å obtained by Bruls *et al.*[17] In the case of $MgGeN_2$, we obtain Mg-N and Ge-N binding distances of 2.10 Å and 1.89 Å, respectively, i.e., the average Mg-N binding distance in $MgGeN_2$ is slightly shorter than in $MgSiN_2$ whereas the average IV-N binding distance is significantly longer in $MgGeN_2$. In AlN, the average Al-N binding distance is 1.90 Å. If we average over the Mg-N and Si-N binding distances in $MgSiN_2$, the resulting average binding distance is 1.94 Å, which is slightly larger than the binding distance in AlN, and if we average over the Mg-N and Ge-N binding distances we find the average binding distance in $MgGeN_2$ to be 2.00 Å.

The orthorhombic structure discussed here is derived from the wurtzite crystal structure by transforming the lattice vectors in the xy-plane as $\boldsymbol{a} = \boldsymbol{a}_1 + 2\boldsymbol{a}_2$ and $\boldsymbol{b} = 2\boldsymbol{a}_1$, while keeping the $\boldsymbol{c}$ lattice vector the same. Here, $\boldsymbol{a}_1$ and $\boldsymbol{a}_2$ are the in-plane lattice vectors of the wurtzite crystal structure, while $\boldsymbol{a}$ and $\boldsymbol{b}$ are the in-plane lattice constants in the orthorhombic structure. The relation between the in-plane lattice constant in wurtzite, a_w, and the a and b lattice constants of the orthorhombic structure is therefore $a_w \approx a/\sqrt{3} \approx b/2$. Note that if pure AlN was calculated using the orthorhombic crystal structure $a_w = a/\sqrt{3} = b/2$. The change from $=$ to $\approx$ is due to relaxations in the $MgSiN_2$ and $MgGeN_2$ systems. It is therefore possible to evaluate an average wurtzite-like lattice constant for the orthorhombic structures as $\bar{a}_w = (a/\sqrt{3} + b/2)/2$. For $MgSiN_2$, the wurtzite-like lattice constant is 3.157 Å, which is only slightly larger (1.0%) than the in-plane lattice constant of wurtzite AlN of 3.127 Å. The corresponding average lattice constant in $MgGeN_2$ is 3.267 Å, which is slightly larger (1.5%) than what is obtained within the PBE approximation for wurtzite GaN (3.218 Å). Furthermore, by using the wurtzite equivalent lattice constant a_w, it is possible to define a deviation from hexagonality in the xy-plane of the orthorhombic structures by evaluating $|a/\sqrt{3} - b/2|/a_w$. In the case of perfect hexagonality, this expression will be zero, and the larger the value becomes the more the orthorhombic structure deviates from the hexagonal structure in the xy-plane. In $MgSiN_2$, this deviation is 5.7%, while it is 3.8% in $MgGeN_2$. $MgSiN_2$, therefore, deviates more from the hexagonal form of the wurtzite crystal structure compared to $MgGeN_2$.

Regarding the out-of-plane lattice constants along the z-direction, we find the c lattice constant in $MgSiN_2$ to be slightly larger than the c lattice constant in AlN, 5.028 Å versus 5.013 Å, respectively. In $MgGeN_2$, the c lattice constant is larger and more similar in size to the corresponding lattice constant in GaN, 5.223 Å in $MgGeN_2$ versus 5.243 Å in GaN. It is therefore clear that the relative volume and other structural properties increase going from AlN to $MgSiN_2$ to $MgGeN_2$, and, furthermore, while the difference between AlN and $MgSiN_2$ is rather small, $MgGeN_2$ is structurally more similar to wurtzite GaN.

Due to the overall structural similarity between $MgSiN_2$ and AlN, as well as between $MgGeN_2$ and GaN, it should be possible to grow epitaxial structures along the c axis composed of $MgSiN_2$ and AlN, as well as structures composed of $MgGeN_2$ and GaN, without significant strain. It is also possible that a small amount of Si substitution on the Ge sites in $MgGeN_2$ will create a situation where the lattice mismatch with GaN vanishes which will be very beneficial when considering the epitaxial growth of heterostructures.

IV. DIELECTRIC TENSORS AND BORN EFFECTIVE CHARGES

The dielectric tensors of $MgSiN_2$, $MgGeN_2$ and AlN are shown in Table III. In the case of $MgSiN_2$ and $MgGeN_2$, we find the dielectric tensor to be anisotropic, with the largest component along the c-axis and the smallest component along the b-axis in the case of $MgSiN_2$. For $MgGeN_2$, the largest component is along the a-axis, while the smallest component is along the b-axis. In both these cases, the a- and c-components are similar in size, while the b-component is much smaller. The absolute values of the dielectric tensor are larger in $MgGeN_2$ compared to $MgSiN_2$ which is related to the reduced band gap in $MgGeN_2$. When comparing the dielectric tensor of $MgSiN_2$ to wurtzite AlN, we find both the a- and b-components to be smaller than the in-plane dielectric constant in AlN. Furthermore, we also find the c-component in $MgSiN_2$ to be smaller than the out-of-plane component in AlN. In Table III, we also show the dielectric tensors of AlN obtained in earlier computational studies, and our calculations are in good agreement with these previous studies.

TABLE III. The dielectric tensor, ε^{∞}, $MgSiN_2$ and wurtzite AlN. Note that the ε_{xx} component for AlN is the in-plane dielectric constant, while the ε_{zz} component is the out-of-plane dielectric constant along the c-axis.

	ε_{xx}	ε_{yy}	ε_{zz}
$MgSiN_2$	4.37	4.29	4.42
$MgGeN_2$	5.12	4.88	5.09
AlN	4.47	…	4.70
AlN[35]	5.17	…	5.36
AlN[36]	4.38	…	4.61

TABLE IV. The Born effective charge tensor $\boldsymbol{Z}^*$ for $MgSiN_2$. The ± and ∓ symbols used for the off-diagonal components represent that each off-diagonal component can be both positive and negative for atoms of the same species, see text for details.

	Mg	Si	N(1)	N(2)
$\boldsymbol{Z}^*_{xx}$	1.92	3.17	−2.04	−3.04
$\boldsymbol{Z}^*_{xy}$	±0.04	∓0.19	∓0.11	±0.47
$\boldsymbol{Z}^*_{yx}$	∓0.04	±0.19	∓0.30	±0.51
$\boldsymbol{Z}^*_{yy}$	1.95	3.02	−2.50	−2.47
$\boldsymbol{Z}^*_{yz}$	±0.01	∓0.20	±0.49	∓0.15
$\boldsymbol{Z}^*_{zy}$	∓0.04	±0.23	±0.49	∓0.13
$\boldsymbol{Z}^*_{zz}$	2.08	3.12	−3.04	−2.16
$\boldsymbol{Z}^*_{xz}$	∓0.02	∓0.05	±0.17	∓0.10
$\boldsymbol{Z}^*_{zx}$	∓0.03	±0.09	±0.19	∓0.04

TABLE V. The Born effective charge tensor $\boldsymbol{Z}^*$ for $MgGeN_2$. The ± and ∓ symbols used for the off-diagonal components represent that each off-diagonal component can be both positive and negative for atoms of the same species, see text for details.

	Mg	Ge	N(1)	N(2)
$\boldsymbol{Z}^*_{xx}$	1.86	3.18	−2.07	−2.98
$\boldsymbol{Z}^*_{xy}$	±0.16	∓0.44	∓0.04	±0.34
$\boldsymbol{Z}^*_{yx}$	∓0.07	±0.31	∓0.33	±0.47
$\boldsymbol{Z}^*_{yy}$	1.97	2.96	−2.48	−2.45
$\boldsymbol{Z}^*_{yz}$	±0.08	∓0.44	±0.41	∓0.11
$\boldsymbol{Z}^*_{zy}$	∓0.11	±0.38	±0.42	∓0.10
$\boldsymbol{Z}^*_{zz}$	2.02	3.15	−2.97	−2.21
$\boldsymbol{Z}^*_{xz}$	±0.01	∓0.09	±0.14	∓0.10
$\boldsymbol{Z}^*_{zx}$	∓0.08	±0.19	±0.16	∓0.02

The Born effective charge tensors in $MgSiN_2$, $MgGeN_2$ and AlN are shown in Tables IV–VI. These charges are related to lattice vibrations and also directly related to the LO-TO splitting, as can be seen in Eq. (1), where larger values for the Born effective charges provide a larger LO-TO splitting, especially in combination with smaller values of the dielectric tensor components. In the case of $MgSiN_2$ and $MgGeN_2$, the Born effective charge tensors are anisotropic with non-negligible off-diagonal elements. We note that the effective charges are sensitive to structural details. In a cubic environment, for example, the effective charges are diagonal and isotropic. However, for non-cubic structures and especially for

TABLE VI. The Born effective charge tensor $\boldsymbol{Z}^*$ for wurtzite AlN.

	$\boldsymbol{Z}^*_{xx}$	$\boldsymbol{Z}^*_{yy}$	$\boldsymbol{Z}^*_{zz}$
Al (N)	2.53	2.53	2.69
Al (N)[35]	2.70	2.70	2.85
Al (N)[36]	2.63	2.53	2.69

systems with complex local environments, non-diagonal and anisotropic effective charges are not surprising.[37] We note that the diagonal elements of the effective charge tensors are similar in $MgSiN_2$ and $MgGeN_2$, where the largest effective charges are found for the Si and Ge atoms in each system. We note that the average of the cation (and anion) diagonal components in $MgSiN_2$, e.g., $\mathbf{Z}^*_{xx} = (\mathbf{Z}^*_{xx}(\mathrm{Mg}) + \mathbf{Z}^*_{xx}(\mathrm{Si}))/2 = (1.92 + 3.17)/2 = 2.545$, is very similar to the effective charges in AlN shown in Table VI.

Regarding the off-diagonal components, we note that these change sign even for atoms of same atomic species such that each off-diagonal component of the tensor is both positive and negative for two atoms of the same species in the unit cell. When averaged over all atoms of the same species in the unit cell, the off-diagonal components become zero and the Born effective charges therefore fulfill the sum-rule $\sum_s \mathbf{Z}^*_{s,ij} = 0$, where s represents the atoms in the unit cell. The sum-rule reflects the fact that when summed over all atoms in the system, each component of the Born effective charge tensor should vanish.

V. Γ-POINT MODES AND RAMAN SPECTRA

We begin the discussion of the lattice dynamics by analysing the vibrations at the Brillouin zone center, i.e., at the Γ-point. The applicable point group for the orthorhombic $Pna2_1$ structure is C_{2v}, and it has four irreducible representations A_1, A_2, B_1 and B_2. We note that A_1, B_1 and B_2 correspond to modes with the same symmetry as a vector along the z, x and y crystal directions, respectively. These are the modes that are subject to a LO-TO splitting according to Eq. (1), while the A_2 modes are unaffected. Since the orthorhombic unit cell contains 16 atoms, there are 48 modes (12 for each symmetry), of which 3 are acoustic with zero frequency at the Γ-point. The zero frequency modes are of A_1, B_1 and B_2 symmetry. The remaining modes are all Raman active. Due to the LO-TO splitting, the frequency of the remaining 11 A_1, 11 B_1 and 11 B_2 modes will depend on the direction from which the Γ-point is approached. That is, as an example, a static field in the z direction will affect the A_1 modes, and therefore, if the Γ-point is approached along the [001] direction, i.e., along the z-axis, the A_1^{LO} mode will be obtained. If the Γ-point is approached along x or y directions, the A_1^{TO} mode will be obtained. In Figs. 3 and 4, we show the calculated frequencies of the Γ-point modes for both $MgSiN_2$ and $MgGeN_2$. These frequencies are also presented in Tables VII and VIII. For both systems, the highest frequency mode along [001], [010] and [100] are A_1^{LO}, B_2^{LO} and B_1^{LO} modes, respectively. In the case of $MgSiN_2$, the highest frequency is found to be $996.4\,\mathrm{cm}^{-1}$ for the A_1^{LO} mode, which is more than $100\,\mathrm{cm}^{-1}$ higher than what we find for the E_1^{LO} mode ($885.4\,\mathrm{cm}^{-1}$) in wurtzite AlN. The A_1^{LO} mode in $MgGeN_2$ is $784.0\,\mathrm{cm}^{-1}$. We note that in the Zn-based II-IV nitrides $ZnSiN_2$, $ZnGeN_2$ and $ZnSnN_2$, the highest frequencies are $980.0\,\mathrm{cm}^{-1}$ (A_1^{LO}),[38] $859.8\,\mathrm{cm}^{-1}$ (B_2^{LO}),[39] and $739\,\mathrm{cm}^{-1}$ (B_2^{LO}),[40] respectively. We therefore note that as the mass of group II and IV elements increases the modes become softer and that both $MgSiN_2$ and $ZnSiN_2$ have modes with significantly higher frequency than found in AlN.

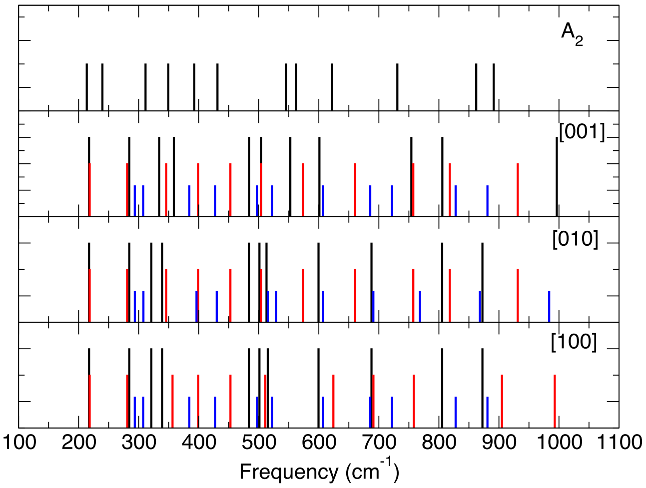

FIG. 3. Calculated phonon modes at the Γ-point of $MgSiN_2$. The top panel contains the A_2 modes. The other panels contain the A_1, B_1 and B_2 modes for $\boldsymbol{q} \rightarrow 0$ along [001], [010], and [100]. A_1, B_1, and B_2 modes are shown using (tall) black, red, and (short) blue bars, respectively.

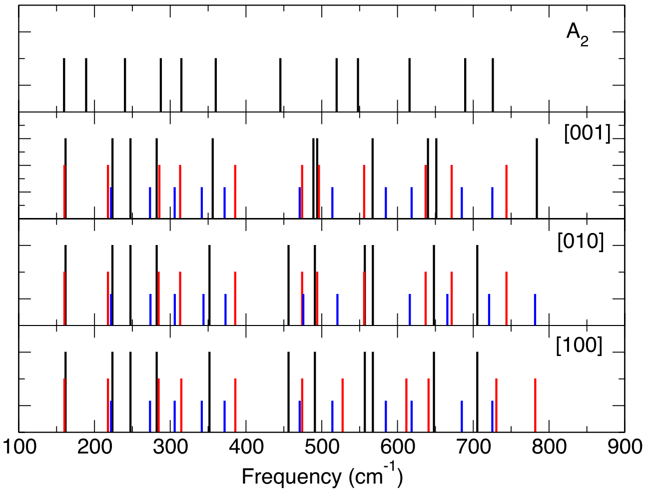

FIG. 4. Calculated phonon modes at the Γ-point of $MgGeN_2$. The top panel contains the A_2 modes. The other panels contain the A_1, B_1 and B_2 modes for $\boldsymbol{q} \rightarrow 0$ along [001], [010] and [100]. A_1, B_1, and B_2 modes are shown using (tall) black, red, and (short) blue bars, respectively.

TABLE VII. Calculated phonon modes at the Γ-point of $MgSiN_2$ sorted according to their symmetry.

A_1^{TO}	A_1^{LO}	B_1^{TO}	B_1^{LO}	B_2^{TO}	B_2^{LO}	A_2
217.4	217.4	218.4	218.4	293.5	293.6	213.6
284.4	284.4	280.8	281.0	307.5	307.9	239.6
321.1	334.2	345.9	356.3	384.3	396.3	311.4
339.0	358.6	398.9	399.2	427.3	430.0	349.4
483.6	483.9	452.7	452.8	496.8	515.1	392.6
501.1	503.9	503.6	510.9	522.1	528.8	431.2
515.1	552.6	573.8	624.3	607.2	607.2	545.2
599.5	601.1	660.6	691.0	685.6	690.8	562.0
687.7	754.1	757.4	758.2	721.9	768.4	622.1
805.5	805.8	818.1	905.0	827.9	868.3	730.8
872.6	996.4	931.3	993.0	880.9	983.7	862.2
						891.3

TABLE VIII. Calculated phonon modes at the Γ-point of $MgGeN_2$ sorted according to their symmetry.

A_1^{TO}	A_1^{LO}	B_1^{TO}	B_1^{LO}	B_2^{TO}	B_2^{LO}	A_2
161.8	161.8	160.3	160.3	221.9	221.9	159.9
223.7	223.8	217.8	217.8	273.3	273.9	189.8
247.5	247.5	285.6	284.7	305.8	306.0	240.2
282.1	282.1	313.1	314.7	341.6	343.9	287.6
351.8	356.0	385.7	385.9	371.8	372.9	314.7
456.2	489.0	474.1	474.2	470.9	475.6	360.1
490.9	494.0	496.3	527.5	514.0	520.7	445.4
556.8	567.2	556.0	611.8	584.6	616.3	519.7
567.5	640.2	637.2	641.0	618.7	665.8	547.9
648.1	651.2	671.5	730.5	684.9	720.9	615.9
705.3	784.0	743.9	781.8	725.2	781.6	689.4
						725.8

Figure 5 shows the results of Raman measurements of a powder sample of $MgSiN_2$, where the principal $MgSiN_2$ peaks are highlighted with their frequency. We note that even though there exist 45 Raman active modes according to the symmetry analysis of $MgSiN_2$, all of them might not show up in Raman measurements since the intensity of some of the peaks might be very low. In addition to the principal peaks, several peaks indicate the presence of free Si in the powder, in keeping with observations made for the Mg/Si_3N_4 synthesis route by Bruls *et al.*[41] Other impurity peaks corresponding to MgO are also present. The impurity peaks were assigned by referring to Raman spectra obtained for the impurity compounds on the same Raman system. As seen in Fig. 5, there are 12 peaks derived solely from $MgSiN_2$ at 225, 329, 354, 408, 567, 623, 712, 751, 833, 893, 917, and 1026 cm^{-1}. These frequencies correspond agreeably with the calculated frequencies of Fig. 3 and Table VII. Especially, these Raman results support the finding that the highest frequency mode in $MgSiN_2$ has a frequency that is significantly higher than the highest frequency found in AlN. Furthermore, we find it to be likely that impurity peaks mask the presence of additional $MgSiN_2$ Raman peaks.

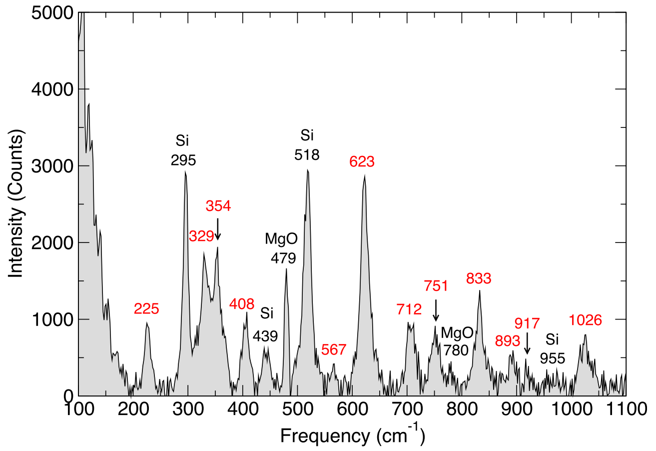

FIG. 5. Measured Raman spectra of a $MgSiN_2$ powder sample. Impurity peaks and assigned frequencies are shown in black. Unique peaks due to $MgSiN_2$ are shown in red.

VI. LATTICE DYNAMICS

Figure 6 shows the phonon dispersions along high symmetry directions in the Brillouin zone of AlN in the wurtzite structure. The lattice dynamics of AlN has already been discussed thoroughly by, for example, Bungaro *et al.*,[35] and we will summarise only some general features of relevance when comparing to the more complex Mg-IV-N_2 systems. The wurtzite unit cell contains 4 atoms and therefore there are 12 modes in the vibrational spectrum. There is a separation centered around 560 cm^{-1} between higher optical modes and the lower energy modes. As was previously mentioned, the highest optical frequency is 885.4 cm^{-1} for the LO mode with E_1 symmetry, which is slightly lower than the experimental frequency[42] of 916 cm^{-1}. We note that the underestimation obtained in the calculations compared to the available Raman frequencies in AlN, shown in Fig. 6, is likely due to the use of the PBE approximation, which tends to underestimate the phonon frequencies found experimentally due to the general underbinding obtained when using this approximation.

By replacing two Al atoms for one Mg and one Si or Ge atom, the size of the system is doubled, but the unit cells for $MgSiN_2$ and $MgGeN_2$ contain 4 formula units (f.u.), as discussed in Sec. III, and the number of phonon modes is therefore 48. As a consequence, the phonon dispersions in $MgSiN_2$ and $MgGeN_2$ shown in Figs. 7 and 8 are much more complex than the dispersions in AlN. In the case of $MgSiN_2$, shown in Fig. 7, we find that the separation found in AlN that centered around 560 cm^{-1} has vanished. Instead, there is a small gap in the vibrations slightly below 800 cm^{-1}. In addition, there are a number of modes with small dispersion just above 800 cm^{-1} that give rise to a tall peak in the phonon density of states shown in Fig. 7. This feature is also found in $ZnSiN_2$,[40] even though the separation between the peak and the lower frequency modes is larger in the case of $ZnSiN_2$. There is, however, a significant difference between the vibrations in $MgSiN_2$ and $ZnSiN_2$: in the latter system, there is a rather significant separation between the modes below 200 cm^{-1} and

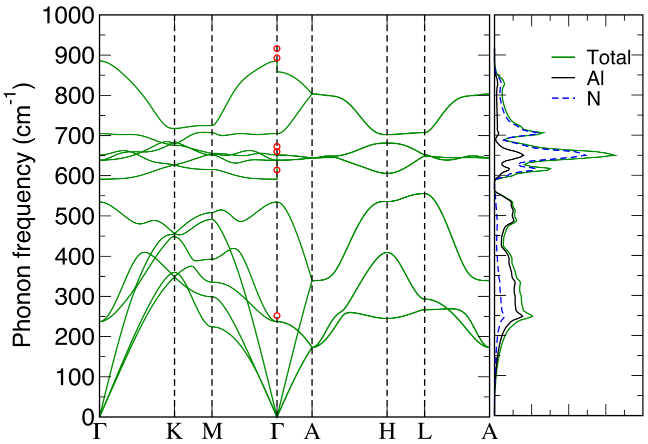

FIG. 6. The calculated phonon dispersions along high symmetry directions in the Brillouin zone (left panel) and the phonon densities of states (right panel) of wurtzite AlN. Experimental Raman frequencies[42] are shown using (red) circles. The phonon densities of states projected onto Al and N atoms are also shown.

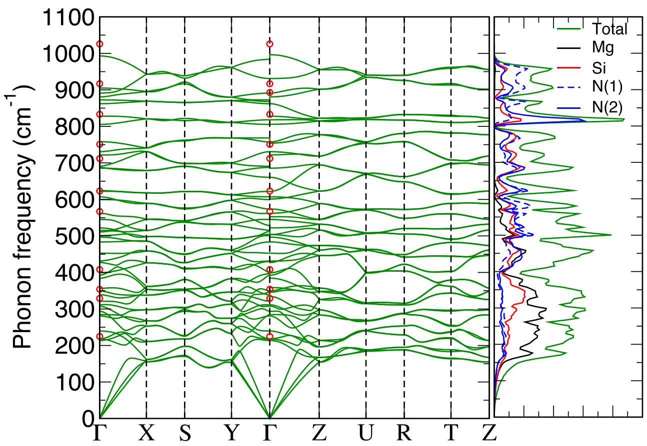

FIG. 7. The calculated phonon dispersions along high symmetry directions in the Brillouin zone (left panel) and the phonon densities of states (right panel) of orthorhombic $MgSiN_2$. Experimental Raman frequencies are shown using (red) circles. The phonon densities of states projected onto Mg, Si, N(1), and N(2) atoms are also shown.

the higher frequency optical modes.[40] In $MgSiN_2$, these two regions have mixed into a single region.

When Si is substituted for the heavier Ge, the lattice vibrations become softer in general, as shown in Fig. 8, and for $MgGeN_2$, the highest frequency is 784.0 cm^{-1}. Compared to $MgSiN_2$, the lattice vibrations in $MgGeN_2$ are more structured with a clear separation between high frequency optical modes and lower frequency modes between 400 cm^{-1} and 440 cm^{-1}. Furthermore, there are two additional gaps, where the lower gap is located at 530 cm^{-1} and the upper gap is located at about 710 cm^{-1}.

In Figs. 6–8, we also present the phonon density of states of AlN, $MgSiN_2$ and $MgGeN_2$ projected onto each atomic species. In AlN, it is clear that cation vibrations dominate at low frequencies and anion vibrations at high frequencies. The same is also true for $MgSiN_2$ and $MgGeN_2$, where in both cases the phonon density of states is dominated by cation vibrations up to about 400 cm^{-1}. Above this point, the vibrations are more dominated by nitrogen vibrations.

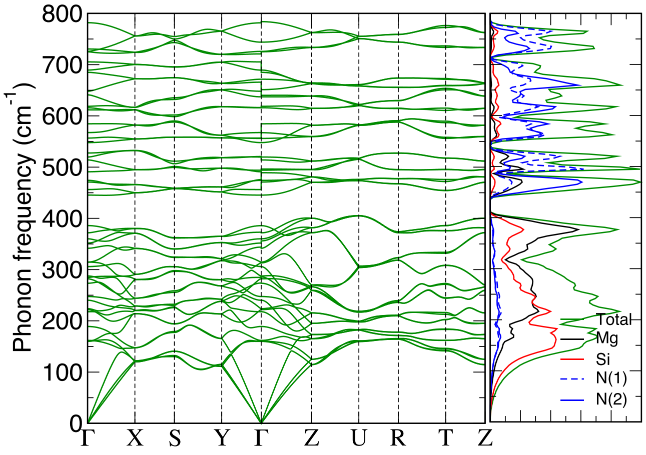

FIG. 8. The calculated phonon dispersions along high symmetry directions in the Brillouin zone (left panel) and the phonon density of states (right panel) of orthorhombic $MgGeN_2$. The phonon densities of states projected onto Mg, Ge, N(1), and N(2) atoms are also shown.

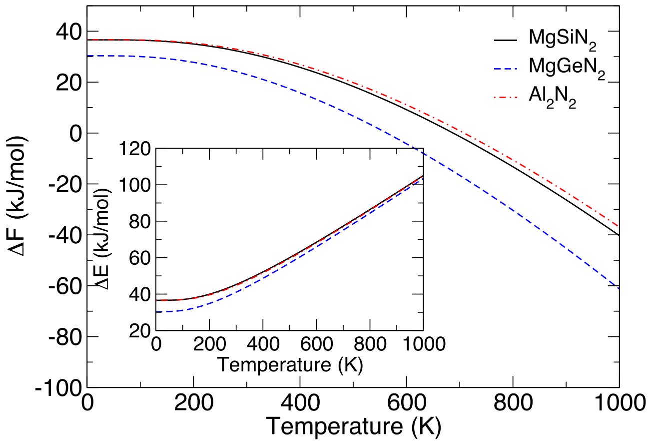

FIG. 9. The calculated Helmholtz free energy and total energy (inset) due to lattice vibrations of $MgSiN_2$, $MgGeN_2$, and AlN.

VII. THERMODYNAMIC PROPERTIES

The contribution of the phonons to thermodynamic properties, such as the Helmholtz free energy F, the total energy E, the specific heat $C_v = (\partial E/\partial T)_v$ and the entropy $S = (E - F)/T$, is expressed through the partition function

$$Z = \Pi_\lambda \frac{e^{-\beta\hbar\omega_\lambda/2}}{1 - e^{-\beta\hbar\omega_\lambda}}, \tag{2}$$

where λ is a combined summation index over both modes and q-points and ω_λ is the vibrational frequency of mode ν at q-point $\boldsymbol{q}$. The Helmholtz free energy is given by

$$F = -\frac{1}{\beta}\ln Z = \sum_\lambda \left[\frac{\hbar\omega_\lambda}{2} + \frac{1}{\beta}\ln\left(1 - \exp(-\beta\hbar\omega_\lambda)\right)\right], \tag{3}$$

and the total energy is given by

$$E = -\frac{\partial \ln Z}{\partial \beta} = \sum_\lambda \hbar\omega_\lambda \left[\frac{1}{2} + \frac{1}{\exp(\beta\hbar\omega_\lambda) - 1}\right]. \tag{4}$$

In Figs. 9 and 10, we show the calculated free energies, total energies, heat capacities and entropies of $MgSiN_2$, $MgGeN_2$ and AlN. Note that in order to facilitate an easier comparison between AlN and the two II-IV nitrides, we have

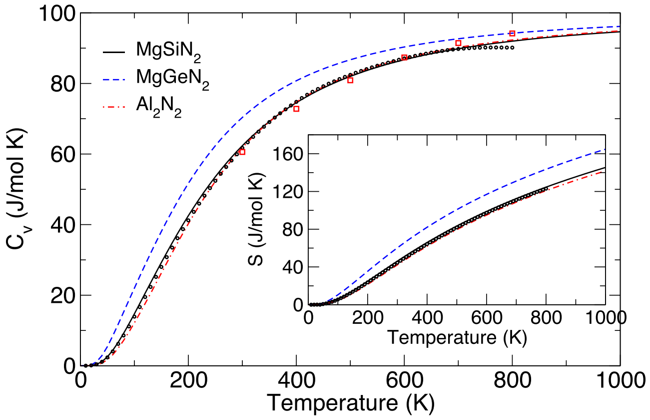

FIG. 10. The specific heat at constant volume and entropy (inset) of $MgSiN_2$, $MgGeN_2$ and AlN. Experimental data for $MgSiN_2$ (black points) and AlN (red squares) are taken from Ref. 19.

plotted the AlN-related curves as if the system is twice as large, i.e., we show the free energy, total energy, heat capacity and entropy for $Al_2N_2 = 2\cdot$ AlN, instead of AlN. Otherwise, all properties shown in Figs. 9 and 10 are about twice as large for $MgSiN_2$ than for AlN.

The zero point energies, i.e., the total energy at $T = 0$ K for $MgSiN_2$, $MgGeN_2$ and AlN is 36.6, 30.3 and 18.3 kJ/mol, respectively, or 0.190, 0.157 and 0.190 eV per nitrogen atom, respectively. In comparison, the calculated zero point energy in $ZnSiN_2$ is 34.0 kJ/mol or 0.176 eV per nitrogen atom,[40] which is slightly less than what is found for $MgSiN_2$ but slightly higher than what is found for $MgGeN_2$. This is expected due to the differences in the mass between Mg, Si, Ge and Zn, where Zn is heavier than Mg, but Ge is heavier than Si and Zn, which makes $MgGeN_2$ a heavier system than both $MgSiN_2$ and $ZnSiN_2$.

The curves for AlN and $MgSiN_2$ follow each other closely in Figs. 9 and 10. The free and total energies of $MgGeN_2$ are smaller than those of $MgSiN_2$; the difference between the free energy of the two compounds increases with temperature, but in contrast, the difference in total energy becomes smaller with increasing temperature. In Fig. 10, it is clear that both the specific heat and the entropy are larger in $MgGeN_2$ compared to $MgSiN_2$. This behaviour is identical to what is observed for Zn-IV-N_2, where the free and total energies decrease from $ZnSiN_2$ to $ZnGeN_2$ to $ZnSnN_2$, while the heat capacity and entropy increase from $ZnSiN_2$ to $ZnGeN_2$ to $ZnSnN_2$.[40]

When comparing our calculated thermodynamic properties to available experimental studies, we find a very good agreement regarding the vibrational entropy in the case of $MgSiN_2$, as is shown in Fig. 10. In Fig. 10, we also show the experimental heat capacity at constant pressure (C_p), which is related to the heat capacity at constant volume (C_v) by

$$C_p - C_v = 9\alpha^2 \frac{V_m T}{\beta_T}, \qquad (5)$$

where α is the thermal expansion, V_m is the molar volume and β_T is the isothermal compressibility. The difference between C_p and C_v is a continuously increasing function of temperature. By using experimental values for the thermal expansion, volume and compressibility, Bruls *et al.*[19] have shown that the difference in the left hand side of Eq. (5) at 800 K is 1.2 J/mol/K, i.e., a relative difference of about 1.3%, which was well inside the accuracy of the measurement. Therefore, for sufficiently low temperatures, the heat capacities at constant pressure and constant volume are approximately the same for $MgSiN_2$, and a comparison between experimental values for the heat capacity at constant pressure and the theoretical heat capacity at constant volume is relevant. As can be seen in Fig. 10, the experimental and theoretical curves follow each other closely up to about 700 K. We note that the calculated curve is slightly higher than the experimental curve for $T \leq 400$ K, after which the experimental curve is higher until this curve flattens at about 700 K.

VIII. SUMMARY AND CONCLUSIONS

We have performed density functional calculations of the structural and lattice dynamical properties of $MgSiN_2$ and $MgGeN_2$. Our calculations are in very good agreement with available experimental results, especially regarding the structural properties, but also regarding thermodynamic properties, i.e., heat capacity and entropy, in the case of $MgSiN_2$. We find that $MgSiN_2$ is structurally very similar to wurtzite AlN, with very good in-plane lattice matching, while $MgGeN_2$ has a larger volume and is more similar to wurtzite GaN. The phonon dispersions in $MgSiN_2$ and $MgGeN_2$ are much more complex than in AlN. We also find that the highest optical mode is about 100 cm^{-1} higher in energy in $MgSiN_2$ compared to AlN, and that the lattice vibrations in $MgGeN_2$ are softer than in both $MgSiN_2$ and AlN. The free energy and the total energy due to lattice vibrations are smaller in $MgGeN_2$ than in $MgSiN_2$, while the opposite is the case for the heat capacity and the entropy. When comparing the thermodynamic properties, i.e., free energy, total energy, heat capacity and entropy, of $MgSiN_2$ and AlN, we find that the curves as a function of temperature follow each other closely with the difference being an approximate factor of 2 per mole. For example, the zero point energy in $MgSiN_2$ is 36.6 kJ/mol, while it is 18.3 kJ/mol in AlN.

ACKNOWLEDGMENTS

We acknowledge support from the Leverhulme Trust via M. A. Moram's Research Leadership Award (RL-007–2012). M. A. Moram further acknowledges support from the Royal Society through a University Research Fellowship. This work used the Imperial College high performance computing facilities and, via our membership of the UK's HEC Materials Chemistry Consortium funded by EPSRC (EP/L000202), the ARCHER UK National Supercomputing Service (http://www.archer.ac.uk).

[1] S. Nakamura, S. J. Pearton, and G. Fasol, *The Blue Laser Diode: The Complete Story* (Springer Verlag, Berlin, Heidelberg, 2000).
[2] M. R. Kramers, O. B. Shchekin, R. Mueller-Mach, G. O. Mueller, L. Zhou, G. Harbers, and M. G. Craford, J. Disp. Technol. **3**, 160 (2007).
[3] U. K. Mishra, S. Likun, T. E. Kazior, and Y. F. Wu, Proc. IEEE **96**, 287 (2008).
[4] R. Elfrink, T. M. Kamel, M. Goedbloed, S. Matova, D. Hohlfeld, Y. van Andel, and R. van Schaijk, J. Micromech. Microeng. **19**, 094005 (2009).
[5] M. Kneissl, T. Kolbe, C. Chua, V. Kueller, N. Lobo, J. Stellmach, A. Knauer, H. Rodriguez, S. Einfeldt, Z. Yang, N. M. Johnson, and M. Weyers, Semicond. Sci. Technol. **26**, 014036 (2011).
[6] J. Wu, J. Appl. Phys. **106**, 011101 (2009).
[7] T. R. Paudel and W. R. Lambrecht, Phys. Rev. B **79**, 245205 (2009).
[8] A. Punya, T. R. Paudel, and W. R. L. Lambrecht, Phys. Status Solidi C **8**, 2492 (2011).
[9] J. B. Quirk, M. Råsander, C. M. McGilvery, R. Palgrave, and M. A. Moram, Appl. Phys. Lett. **105**, 112108 (2014).
[10] M. Råsander and M. A. Moram, Mater. Res. Express **3**, 85902 (2016).
[11] A. P. Jaroenjittichai and W. R. L. Lambrecht, Phys. Rev. B **94**, 125201 (2016).
[12] J. David, Y. Laurent, and J. Lang, Bull. Soc. Fr. Mineral. Cristallogr. **93**, 153 (1970).
[13] C. M. Fang, R. A. de Groot, R. J. Bruls, H. T. Hintzen, and G. de With, J. Phys.: Condens. Matter **11**, 4833 (1999).
[14] J. Y. Huang, L.-C. Tang, and M. H. Lee, J. Phys.: Condens. Matter **13**, 10417 (2001).
[15] T. de Boer, T. D. Boyko, C. Braun, W. Schnick, and A. Moewes, Phys. Status Solidi RRL **9**, 250 (2015).
[16] G. K. Gaido, G. P. Dubrovskii, and A. M. Zykov, Izv. Akad. Nauk. SSSR, Neorg. Mater. **10**, 564 (1974).

[17] R. J. Bruls, H. T. Hintzen, R. Metselaar, and C.-K. Loong, J. Phys. Chem. Solids **61**, 1285 (2000).
[18] R. J. Bruls, H. T. Hintzen, and R. Metselaar, J. Euro. Ceram. Soc. **25**, 767 (2005).
[19] R. J. Bruls, H. T. Hintzen, R. Metselaar, and J. C. van Miltenburg, J. Phys. Chem. B **102**, 7871 (1998).
[20] F. Arab, F. A. Sahraoui, K. Haddadi, A. Bouhemadou, and L. Louail, Phase Trans. **89**, 480 (2016).
[21] S. Pramchu, A. Punya Jaroenjittichai, and Y. Laosiritaworn, Ceramics International **43**, S444–S448 (2017).
[22] P. E. Blöchl, Phys. Rev. B **50**, 17953 (1994).
[23] G. Kresse and J. Furthmüller, Phys. Rev. B **54**, 11169 (1996).
[24] G. Kresse and D. Joubert, Phys. Rev. B **59**, 1758 (1999).
[25] J. P. Perdew, K. Burke, and M. Ernzerhof, Phys. Rev. Lett. **77**, 3865 (1996).
[26] L. Chaput, A. Togo, I. Tanaka, and G. Hug, Phys. Rev. B **84**, 094302 (2011).
[27] K. Parlinski, Z. Q. Li, and Y. Kawazoe, Phys. Rev. Lett. **78**, 4063 (1997).
[28] R. M. Pick, M. H. Cohen, and R. M. Martin, Phys. Rev. B **1**, 910 (1970).
[29] P. Giannozzi, S. Degironcoli, P. Pavone, and S. Baroni, Phys. Rev. B **43**, 7231 (1991).
[30] X. Gonze and C. Lee, Phys. Rev. B **55**, 10355 (1997).
[31] Y. Wang, J. J. Wang, W. Y. Wang, Z. G. Mei, S. L. Shang, L. Q. Chen, and Z. K. Liu, J. Phys.: Condens. Matter **22**, 202201 (2010).
[32] S. Baroni and R. Resta, Phys. Rev. B **33**, 7017 (1986).
[33] M. Gajdoš, K. Hummer, G. Kresse, J. Furthmüller, and F. Bechstedt, Phys. Rev. B **73**, 045112 (2006).
[34] M. Råsander and M. A. Moram, J. Chem. Phys. **143**, 144104 (2015).
[35] C. Bungaro, K. Rapcewicz, and J. Bernholc, Phys. Rev. B **61**, 6720 (2000).
[36] K. Karch and F. Bechstedt, Phys. Rev. B **56**, 7404 (1997).
[37] E. Cockayne and B. P. Burton, Phys. Rev. B **62**, 3735 (2000).
[38] T. R. Paudel and W. R. L. Lambrecht, Phys. Rev. B **76**, 115205 (2007).
[39] W. R. L. Lambrecht, E. Alldredge, and K. Kim, Phys. Rev. B **72**, 155202 (2005).
[40] T. R. Paudel and W. R. L. Lambrecht, Phys. Rev. B **78**, 115204 (2008).
[41] R. J. Bruls, A. A. Kudyba-Jansen, P. Gerharts, H. T. Hintzen, and R. Metselaar, J. Mater. Sci. Mater. Electron. **13**, 63 (2002).
[42] L. E. McNeil, M. Grimsditch, and R. H. French, J. Am. Chem. Soc. **76**, 1132 (1993).